AAS-26-167

APOLLO 11 LUNAR MODULE TOUCHDOWN DYNAMICS RECONSTRUCTION VERIFICATION AND VALIDATION FOR HUMAN LANDING SYSTEMS

Rekesh M. Ali,[*] Adam C. Slagle,[†] and Alessandro Mordasiewicz, [‡]
Juan Orphee, [§] and Peter J. McDonough [**]

This paper presents an updated high-fidelity lunar landing dynamics simulation test bed developed at NASA Marshall Space Flight Center (MSFC) in support of the Human Landing System (HLS) program, with verification support from NASA Langley Research Center (LaRC). The MSFC GeneraLized Aerospace Simulation in Simulink® (GLASS) program uses MATLAB®/Simulink® and Simscape™ Multibody™ to model detailed contact dynamics of lunar regolith, shock absorbers, footpads, and multibody linkages, laying the groundwork for integrated analyses incorporating in-the-loop guidance, navigation, and control systems. For validation, the simulation focuses on pure landing dynamics and is benchmarked against Apollo 11 flight data and independent modern reconstructions.

The GLASS simulation demonstrates excellent agreement with historical Apollo data, validating the approach against real-world landing dynamics. Further, strong correlation between the MSFC and LaRC simulation results across different platforms provides verification of the modeling methodology. This collaborative effort establishes confidence in the simulation framework and provides a solid foundation for comprehensive HLS system analysis. The paper details the modeling methodology, validation against Apollo data, and verification through comparison with Zupp's reconstruction and LaRC's MSC Automated Dynamic Analysis of Mechanical Systems (Adams) reconstruction results.

INTRODUCTION

NASA's Artemis missions aim to return humans to the Moon and establish a sustained presence as part of the agency's Moon-to-Mars initiative.[1] This effort coincides with a broader global resurgence in lunar activity. The pace of lunar landing attempts has accelerated in the 2020s, with

---

[*] Aerospace Engineer, EV42 Guidance, Navigation, and Mission Analysis Branch, Amentum Space Exploration Division (ASED)/Mclaurin Aerospace, Knoxville, TN 37906

[†] Aerospace Engineer, Mechanical Systems Branch, NASA Langley Research Center, Hampton, VA 23681

[‡‡] Summer Aerospace Intern, EV42 Guidance, Navigation, and Mission Analysis Branch, Amentum Space Exploration Division (ASED)/Purdue University, West Lafayette, IN 47907

[§] HLS GN&C Lead, EV41 Control Systems Design and Analysis Branch, NASA Marshall Space Flight Center, Huntsville, AL 35812

[**] ESSCA Team Lead, EV42 Guidance, Navigation, and Mission Analysis Branch, Amentum Space Exploration Division (ASED), Hunstville, AL 35812

participation from multiple nations and commercial providers. Despite rapid progress, the success rate of unmanned lunar landing attempts is on the order of 50% over the past decade.[*]

Landing on the Moon remains challenging because sites are unprepared and must be characterized largely from orbital data. Touchdown outcomes are governed by local topography and regolith properties, which set the boundary conditions for contact dynamics and tip-over potential. Site selection is therefore critical, yet current orbital terrain products at candidate polar locations are limited to multi-meter scale pixels, leaving substantial unresolved structure at scales relevant to the lander footprint.[2] This motivates analysis tools capable of quantifying landing performance across uncertain terrain and soil conditions.

For high-risk systems, performance is typically assessed using high-fidelity, nonlinear, multibody simulations that capture the coupled response of vehicle dynamics, landing gear, and surface interaction. Within the Human Landing System (HLS) program, NASA maintains independent analysis models to evaluate commercial lander designs against mission and human-rating requirements. Multiple independent tools and teams are used to reproduce critical flight dynamics and loads, and cross-verification is used for confidence building and error identification. This independent cross-verification approach is a cornerstone of NASA's risk minimization posture.[3,4]

This paper is concerned with high-fidelity dynamical modeling of the touchdown event beginning at first surface contact and extending through subsequent stabilization or tip-over. The Apollo Lunar Module serves as the development test article due to the abundance of information available on its design specification and flight history. The implementation detailed herein is an updated touchdown dynamics capability within NASA MSFC's MATLAB®/Simulink® and Simscape™ Multibody™-based HLS model, known as GLASS,[5] with verification support and reference material informed by NASA LaRC's MSC Adams-based efforts. Model verification and validation (V&V) is established through comparison to the Apollo 11 landing event using digitized flight measurements and modern reconstruction results.

LANDING DYNAMICS

The landing objective is to place the vehicle upon the lunar surface in a manner that preserves the safety of the crew and integrity of the vehicle, enabling mission operations and ensuring the capability to depart. A lander begins in a low-altitude parking orbit in the inclination plane of the desired landing site. It de-orbits into a descent trajectory that intersects with the surface. At touchdown, the vehicle retains some relative motion with respect to the surface, introducing the need for passive energy absorption. Uncertainty in the local topography and mechanical properties of the landing site creates challenges for contact dynamics and tip-over stability.[6,7]

The greatest risks to mission and crew are impact loads and toppling potential. Loads initiate at the footpads and propagate through the shock absorbers and primary structure to inform attitude dynamics. The landing gear is therefore the primary subsystem that must be robust to the range of vehicle impact states and landing site geometries and material compositions expected in flight. Its design ultimately sets the bounds on performance under these uncertainties.[8]

The present work focuses on contact modeling and passive energy absorption during touchdown on simple flat planes. Other contributors to end-to-end landing risk—such as in-the-loop GN&C,

---

[*] NASA, "Moon Missions, URL: https://science.nasa.gov/moon/missions/ [retrieved 8 Dec. 2025].

propellant slosh, RCS, digital elevation maps, hazard representation, plume-to-surface interaction, and flexible-body dynamics—are acknowledged but are outside the scope of this paper.

APOLLO LUNAR MODULE

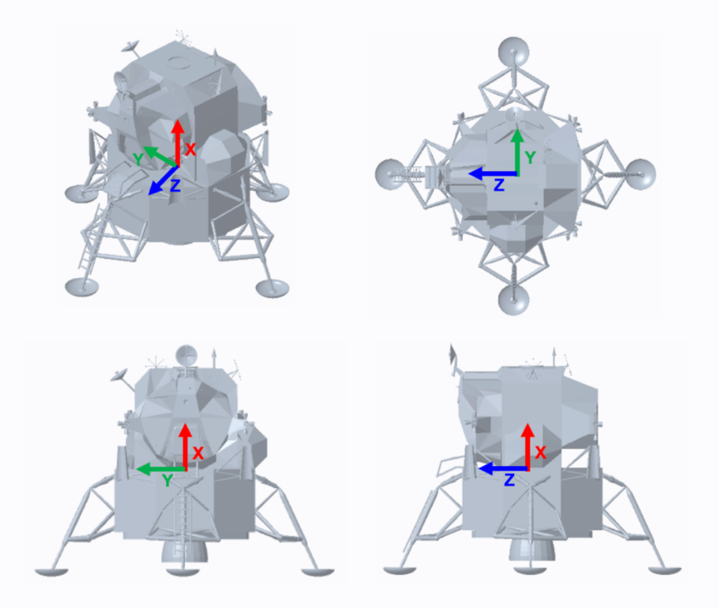

Figure 1. Apollo Lunar Module CAD model and body frame.

The subject of this study is the Apollo Lunar Module (LM), which made six successful lunar landings over its employment from 1969 to 1972, on missions Apollo 11, 12, and 14–17. Figure 1 shows the vehicle in the deployed configuration, including the body coordinate system used in this work. These illustrations are captured from the publicly available NASA computer aided design (CAD) model.[*] The attitude convention follows an aircraft-style notation: yaw about +X, pitch about +Y, and roll about +Z.

Table 1. Apollo LM mass properties.

Parameter	Nominal	Apollo 11	Unit
Total Vehicle Mass	7,063.5	4,932	kg
Primary Strut Mass	43.1	43.1	kg
Primary Inner Piston Mass	13.6	13.6	kg
Secondary Strut Mass	5.12	5.12	kg
Footpad Mass	11	11	kg
CG Height Above Footpad Bottom (+X)	3.62	3.62	m
Roll Moment of Inertia at CG (XX)	16,492	7,953	kg/m^2
Pitch Moment of Inertia at CG (YY)	17,409	6,332	kg/m^2
Yaw Moment of Inertia at CG (ZZ)	20,800	5,879	kg/m^2

---

[*] NASA, "Apollo Lunar Module," *NASA Science* (3D Resources web page), last updated June 9, 2025. https://science.nasa.gov/3d-resources/apollo-lunar-module/.

Touchdown mass properties depend strongly on the remaining propellant at landing. Apollo 11 made a comparatively light landing near propellant depletion (approximately 20 s remaining), resulting in a substantially lower total mass and inertia than a nominal configuration. Two mass property sets are carried in this work because the V&V comparisons use two independent reference simulations with different assumptions. The Zupp comparison uses nominal mass properties, while the MSC Adams comparison uses Apollo 11 mass properties.[9] Table 1 lists the mass properties used for each case.

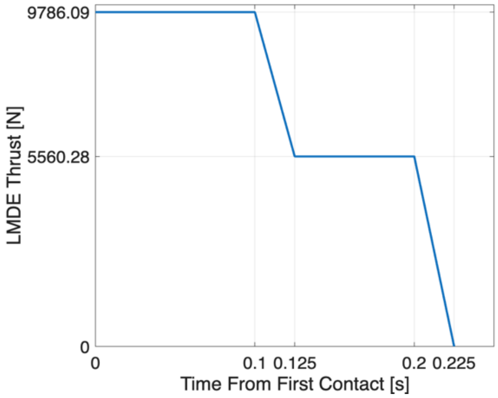

Figure 2. Apollo 11 Lunar Module Descent Engine tail-off thrust.

The vehicle is outfitted with the LM Descent Engine (LMDE) to generate lift during descent. The Apollo 11 LM made contact with the surface before the LMDE had fully shut down. Figure 2 shows the reconstructed tail off thrust time history from the moment of touchdown onward. This reconstruction ignores any thrust amplification effects that may have occurred due to proximity with the surface. Due to the limited gimbaling range,[10] it is assumed that this thrust acts through the body +X axis at the center of mass.

APOLLO LANDING GEAR

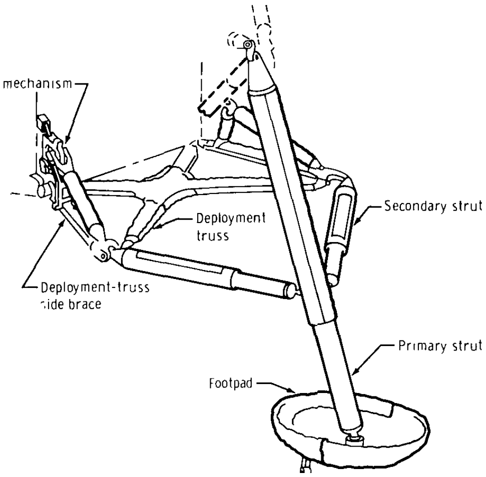

Figure 3. Landing gear isometric detail view.

The composition of a landing gear typically adopts a truss-based layout, using a triad of linear attenuators in a kinematically stable linkage to absorb loads across any vehicle heading. The Apollo LM landing gear sports a cantilever configuration: a primary strut, braced at mid-span by two secondary struts, with the stroking member of the primary cantilevered from the point where the three struts intersect. An isometric view of the Apollo LM landing gear is shown in Figure 3. The primary struts are well positioned to absorb loads in the vertical direction while the secondaries moderate loads in the lateral directions. Universal joints connect the truss elements to allow for linear motion of the dampers and to mitigate unfavorable shear moments in linkage cross sections. A crescent shaped footpad on a spherical joint terminates the free end of the cantilever. The footpad is convex to the surface to discourage excessive plowing and reduce the likelihood of catching under superficial obstructions.

Table 2. Landing gear geometric parameters.

Parameter	Description	Value	Unit
r_{ftpd}	Footprint radius	4.242	m
r_{truss_upper}	Truss radius upper	3.061	m
r_{truss_lower}	Truss radius lower	2.996	m
h_{upper}	Upper truss height	2.874	m
h_{lower}	Lower truss height	1.19	m
h_{ftpd}	Footpad height (base to ball joint)	0.10	m
w_{sec}	Secondary truss width	2.239	m
l_{conn}	Prim-sec connection length	1.157	m

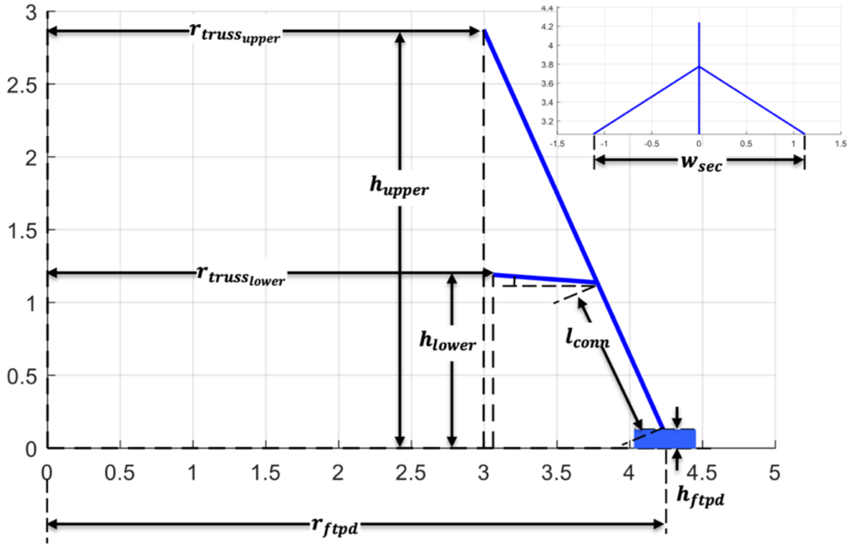

Figure 4. Landing gear schematic.

The Apollo LM carries four landing gear legs arranged symmetrically about the vehicle yaw axis. Landing gear geometry is driven by toppling stability margins and by the need to provide adequate clearance of the descent engine nozzle to surface obstructions. The landing gear geometry is parameterized in Table 2 using the schematic shown in Figure 4. The figure represents a projection of the deployed configuration onto planes. The annotations shown are the minimum set of measurements required to reconstruct the landing gear geometry. These values were measured in CAD using the official NASA Apollo LM model. Qualitative spot checks against landing gear schematics in the Apollo Experience Report (Reference 7) indicate the approximated geometry is satisfactory for this study.

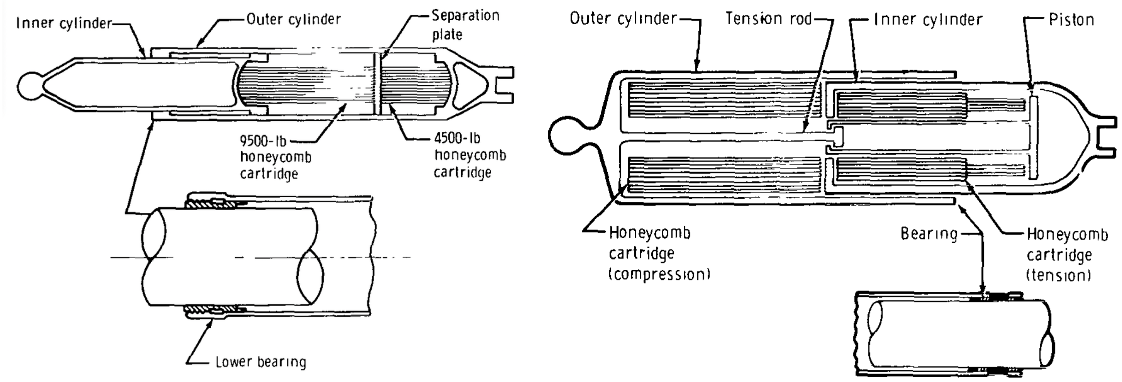

Figure 5. Honeycomb attenuator axial crosscuts. Primary (left), secondary (right).

The telescoping linear attenuators function like dashpots, using crushable aluminum honeycomb cartridges as the energy absorption mechanism. These expendable aluminum cores are machined to provide a predictable load response under plastic deformation. Through this crush-core action, the vehicle is lightly decoupled from its landing gear, and the transmitted loads are limited to the deformation strength of the honeycomb. Figure 5 depicts axial crosscuts of the primary and secondary strut attenuation mechanisms. The primary struts stroke in compression only, whereas the secondary struts provide load mitigation in both compression and tension. Contact bearings bridge the cylinder and piston, regulating friction to allow for reliable relative motion.

Table 3. Honeycomb attenuator mechanical properties.

Parameter	Value	Unit
Primary Compression Stroke Limit	0.812	m
Primary Compression Stroke Length (Stage 1)	0.254	m
Primary Compression Stroke Length (Stage 2)	0.558	m
Primary Compression Deformation Load (Stage 1)	20,017	N
Primary Compression Deformation Load (Stage 2)	42,358	N
Secondary Compression Stroke Limit	0.305	m
Secondary Compression Deformation Load	20,017	N
Secondary Tension Stroke Limit	0.407	m
Secondary Tension Stroke Length (Stage 1)	0.102	m
Secondary Tension Stroke Length (Stage 2)	0.305	m
Secondary Tension Deformation Load (Stage 1)	2,224	N
Secondary Tension Deformation Load (Stage 2)	22,241	N
Contact Bearing Coefficient of Friction	0.23	

The reaction force from a honeycomb core is designed to remain approximately constant over the entirety of its crushable length. Multiple loading stages are implemented in the Apollo LM landing gear by stacking cores of different lattice density or cross-sectional area into a single cartridge. Table 3 lists the stroke limits and corresponding deformation loads for all stages of the primary and secondary struts. For multi-stage cartridges, the first stage expends before the second because it is designed with a lower deformation strength. The crushable lengths of all stages sum to the total stroke limit in that direction. Both struts are assumed to share a similar coefficient of friction due to lateral forces acting on the interior contact bearings.

SIMULATION DEVELOPMENT

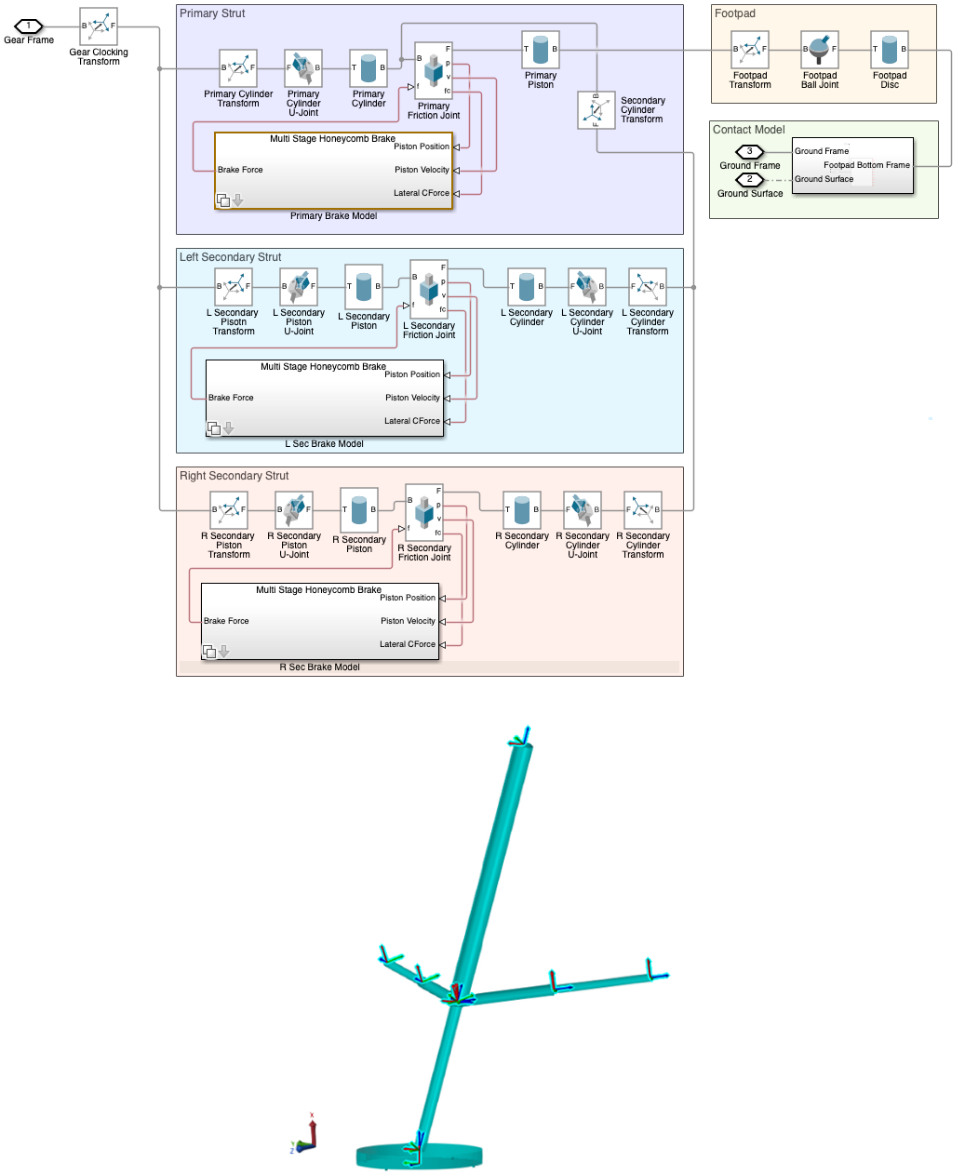

Figure 6. Simscape™ landing gear model block diagram and single landing gear with frames.

The landing gear dynamics are implemented in MATLAB® using Simulink® and Simscape™ Multibody™. Simscape Multibody is used to program the constrained dynamics of the cantilever landing gear assemblage while Simulink® Function blocks provide the nonstandard forcing functions associated with the honeycomb attenuators and regolith contact forces. The overall model structure of the landing gear is laid out in a high-level Simulink® block diagram in Figure 6, which links the primary and secondary structs from the vehicle attach frame to the footpad and contact model. This block representation offers stronger intuition for how the elements are coupled than a traditional code implementation.

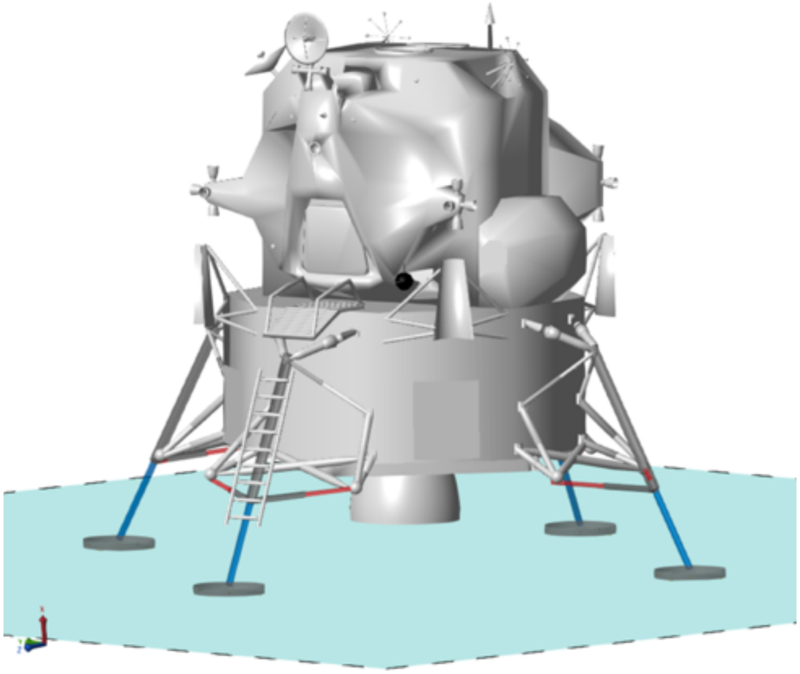

Figure 7. Apollo Lunar Module CAD with Simscape™ landing gear on flat contact plane.

The model is parameterized to be generic, allowing for polymorphic geometries without altering the underlying structure. Figure 7 shows the native Simscape™ visualization of the Apollo CAD model with all 4 landing gear legs assembled and resting on a flat contact plane.

Simscape™ provides a variety of solvers for its physical networks. In the landing scenario studied here, the system alternates between long intervals of smooth motion and brief phases of impact where the problem stiffness increases sharply. The severity and duration of those stiff windows vary with initial conditions and contact configuration—uncertainty which makes a variable timestep solver desirable. Additionally, Simscape™ physical networks with constrained degrees-of-freedom (DOF) lead to equations of motion with coupled differential algebraic equations (DAE). Constrained motion and large step sizes have better convergence and stability when propagated with an implicit solver due to higher stability bounds by solving for future states coupled and directly.[11] Simscape™'s *daessc* solver specifically supports DAE networks and automatically refines the timestep based on specified error tolerances.[12]

Achieving suitable performance with *daessc* requires attention to Jacobian evaluation, error tolerances, and state scaling. When portions of the model—such as custom force laws—are implemented using MATLAB® Function blocks, the solver cannot form a fully analytical global Jacobian and must instead approximate it numerically via state perturbations.[13] This is costly because it requires residual re-evaluations for each perturbation, so the computational burden grows non-linearly with the number of states and constraints. Performance can degrade further during contact episodes that drive repeated step rejections, smaller step sizes, and more frequent Jacobian updates. In this landing gear model, zero-crossing events in compliant elements led to high frequency force reversals that were a recurring source of solver churn. Adding a small amount of viscous damping to all joints, on the order of 5-10 N-s/m, reduced chatter and improved convergence by encouraging joint velocities toward zero during settling. This is especially beneficial in the footpad joints where competing contact spring forces produced high sensitivity to orientation.

Error tolerance and state scaling serve as tuning knobs for trading accuracy against runtime. Higher tolerances loosen the timestep refinement error threshold, reducing computational cost at the expense of accuracy.[14] The tolerances measure error against the normalized state vector that Simscape™ generates automatically. The state normalization scalars can be configured as nominal values. Scaling by these nominal values normalizes state magnitudes toward $O(1)$, which reduces skew in the solver Jacobian, improving the numerical conditioning and convergence efficiency of the Newton iterations.

HONEYCOMB MODEL

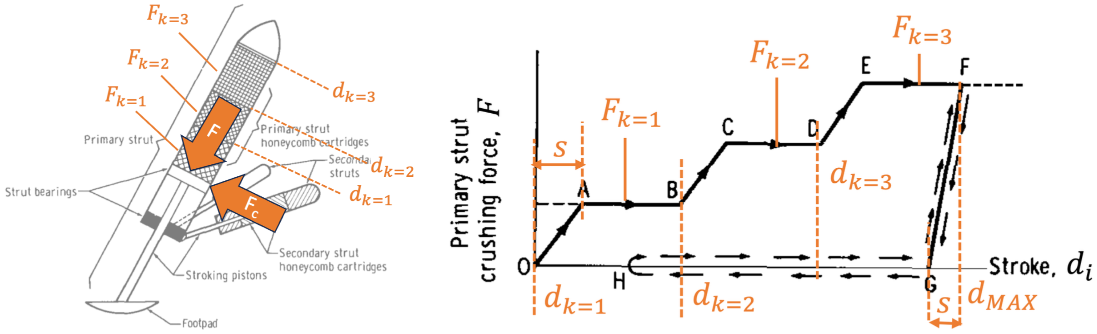

Figure 8. Honeycomb model free-body diagram (left) and load-stroke diagram (right).

The honeycomb brake model is straightforward in its plumbing. Prismatic joints permit 1-DOF translational motion and provide position, velocity, and wall normal forces of the piston-to-cylinder interface. These outputs are ingested by the brake model which computes the response load based on the honeycomb design parameters. The response load is routed back into the joint to provide the dynamic reaction. While the brake response corresponds to the honeycomb crush level, a direct force lookup from the load-stroke table is insufficient for two reasons: discrete stage steps introduce force discontinuities that are undesirable for numerical stability, and elastic loading/unloading is path dependent that requires memory of the crushed interface.[15] Both effects are handled during execution using smooth transition activation functions. The brake force, F, acts to resist motion and is written as

$$F = w_L[F_k + w_S(F_{k+1} - F_k)] + \mu_B F_c \tag{1}$$

where F_k is the current stage level load, F_{k+1} is the next stage load, w_S is the stage transition weight, and w_L is the load/unload weight. The term $\mu_B F_c$ represents additional resistance from contact friction in the bearings proportional to the cylinder wall constraint force. The left side of Figure 8 shows the free-body diagram that this equation represents.

The hyperbolic tangent is used for both activations because it is continuous and differentiable. The stage-to-stage transition, w_T, occurs across a prescribed transition width, s. Letting d_i denote the instantaneous strut stroke and d_{k+1} denote the following stage stroke boundary,

$$w_S = \frac{1}{2}\left[1 - \tanh\left(\frac{6}{s}\left([d_{k+1} - d_i] - \frac{s}{2}\right)\right)\right] \tag{2}$$

Here, w_S smoothly rises from near 0 to near 1 as the stroke advances through the transition region, allowing the crush load to ramp from F_k to F_{k+1}. When a transition region has been fully traversed, the stage stroke boundary latches to the next level which prevents the force from reverting to a previous level. This transition weight is illustrated in the load-stroke diagram of Figure 8 in segments 0⇒A, B⇒C, and D⇒E.

The second weight, w_T, handles the path dependent load/release behavior based on the cartridge's crushed interface d_{MAX}. Using the same transition width s,

$$w_L = \frac{1}{2}\left[1 - \tanh\left(\frac{6}{s}\left([d_{MAX} - d_i] - \frac{s}{2}\right)\right)\right] \tag{3}$$

In this expression w_L is near 1 while the strut remains near its maximum stroke and decays smoothly toward 0 as it retracts beyond the transition width. The brake behaves like an elastic element over the transition band with an effective stiffness $K_{\text{brake}} \approx F_k/s$. Therefore, s sets a characteristic frequency for the landing gear and can introduce harmonics in the simulation. Since the design elasticity width is unknown, a value of $s = 1$ mm is used to balance numerical stability and stage sharpness. This transition makes up segment F⇒G in the load-stroke diagram of Figure 8.

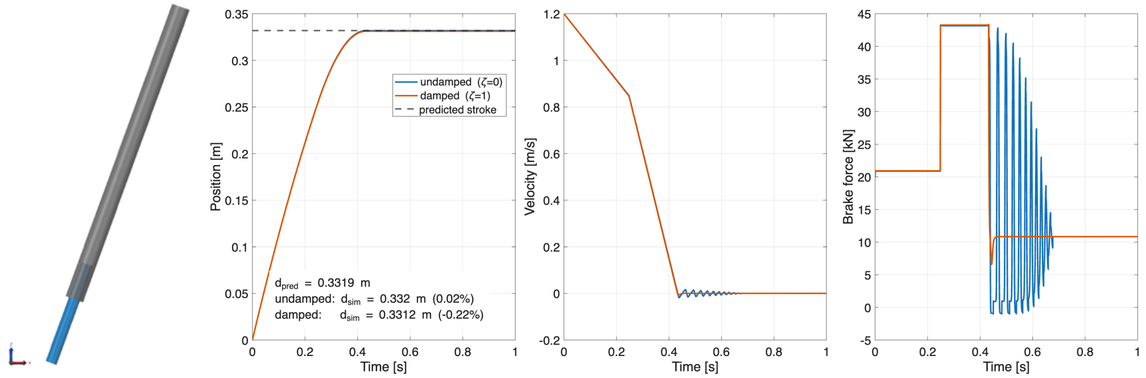

Figure 9. Honeycomb attenuator model verification exercise.

The crush model verification is shown in Figure 9. Consider a simple setup under lunar gravity of 1.63 m/s^2 where the cylinder has a mass of 7,063.5 kg and initial stroking velocity of 1.2 m/s. It is angled at 20° to ensure some measure of wall normal force to activate the bearing friction. The resulting stroke follows from conservation of energy by equating the initial kinetic and gravitational potential energy to the work dissipated by each stage of the strut and bearing contact friction,

$$mg\cos\theta\,(d_1 + d_2) + \frac{1}{2}mv^2 = F_1 d_1 + F_2 d_2 + \mu_B mg\sin\theta\,(d_1 + d_2) \tag{4}$$

For the parameters used here, assume d_1 is already known because the first stage fully expends. The energy balance is thus used to solve for d_2. The resulting predicted total stroke is 0.3319 m, and the simulation matches it with a 0.02% error. The blue curve corresponds to the brake model as previously described and exhibits ringing after the stroke reaches its final value because of the elasticity introduced by the loading transition.

In principle the bearing friction helps to subdue oscillations, however it is not significant enough in this example. Since the characteristic frequency of the honeycombs are unknown, and since vibrational loads are not a subject of the validation study, these harmonics are undesirable from a solver performance standpoint. An additional damping term on the strut velocity can help to attenuate the number of elastic cycles, shown by the red curve with a damping ratio $\zeta = 1$. The damping coefficient is computed using the canonical second order mass-normalized form, $c = 2\zeta\omega$, where $\omega = \sqrt{K_{brake}/m_{total}}$ corresponds to the maximum stage load and total vehicle mass. To stay consistent with the design loading table, the sum of the transition load and damping are saturated at the force corresponding to the current crush stage. As can be seen with the red curve, the load-stroke behavior is conserved and achieves a rest condition in considerably fewer cycles.

CONTACT MODEL

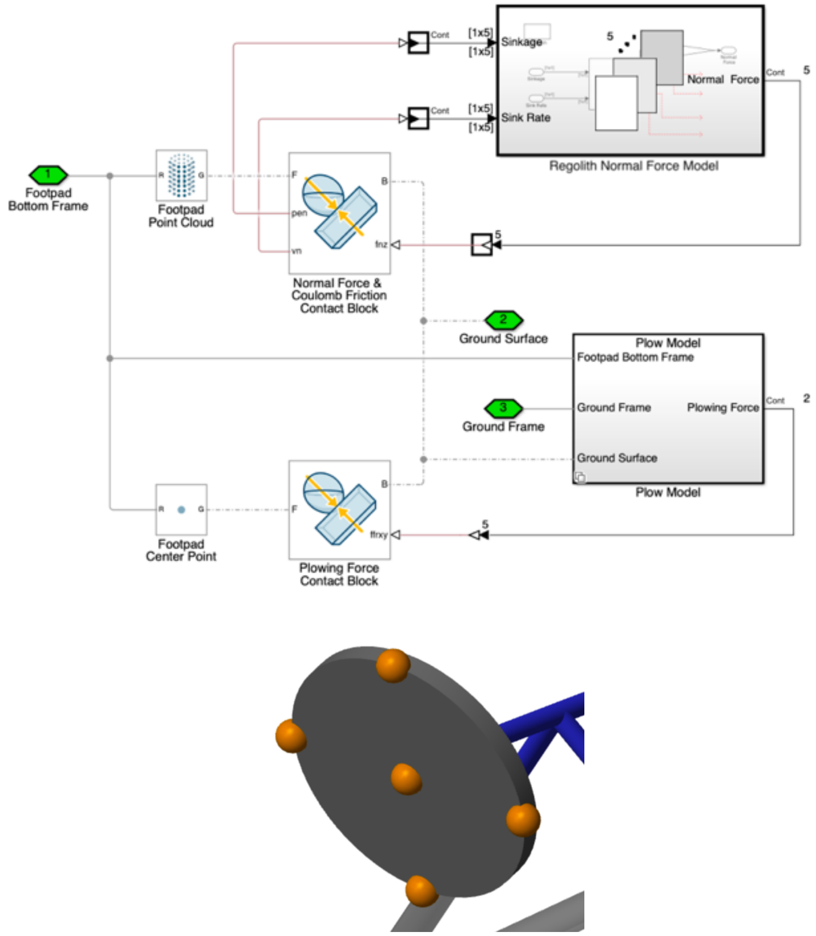

Figure 10. Simscape™ contact model diagram and footpad point cloud.

The contact model is responsible for generating terrain reaction forces as the footpads interact with the surface. This is achieved by tracking the penetration state of the footpad interface within the surface geometry and mapping that state back to a reaction through custom force laws. The Simulink® diagram in Figure 10 illustrates the components used in the implementation. The footpad interface is represented by a point cloud rigidly attached to the bottom of a disc. Each disc includes one contact point at the center and four contact points evenly spaced along the perimeter, as shown in Figure 10. The ground surface for this study, not pictured in the diagram, is an Infinite Plane block that can be inclined to represent sloped terrain. Contact state information is provided by the Spatial Contact Force block for each individual point. Its outputs are routed into the contact force laws, which in turn generate the independent reactions. The contact block then lumps these reactions internally to apply the net force and moment that drive the dynamics.

During the Apollo program, the Bendix Corporation developed a comprehensive footpad-to-soil interaction model based on extensive empirical testing and analysis.[16] This high-fidelity model breaks the reaction into components parallel and perpendicular to the footpad instantaneous velocity. The parallel component is a function of the soil mechanical strength and momentum transfer effects, while the perpendicular component is proportional by a dimensionless factor related to contact area projections, footpad surface-to-velocity angle, and depth of penetration. The Bendix model was incorporated into landing dynamics simulations to predict LM touchdown behavior across a variety of lunar terrain.

Apollo 11 mission photography later revealed that footpad translation and penetrations were small enough that a simplified model would be adequate to capture the relevant dynamics to first-order. Zupp uses this observation to simplify the Bendix model into components normal and tangential to the footpad surface. The normal reaction, F_n, is driven by the bearing strength of the surface, K_n, as a function of penetration depth, δ_n. Zupp neglects Bendix's damping-like behavior of the momentum transfer term. The tangential reaction, F_t, includes a Coulomb friction term, μF_n, and an additional component, $K_p \delta_t$, that represents the linear plowing resistance as soil builds up against the leading edge of the footpad during lateral motion.

$$F_n = \begin{cases} K_n \delta_n, & \delta_n < 0 \\ 0, & \delta_n \geq 0 \end{cases}$$
$$F_t = \mu F_n + K_p \delta_t \tag{5}$$

The Zupp regolith parameters used in this study are summarized in Table 4. Zupp obtained these values by inferring penetration and slide-out bounds from Apollo 11 landing-site photography, then iterating K_n, μ, and $K_p$in simulation until predictions matched values derived from the imagery. Because the model is a local linearization around the Apollo 11 reconstruction conditions, these parameters are valid only near that operating regime.

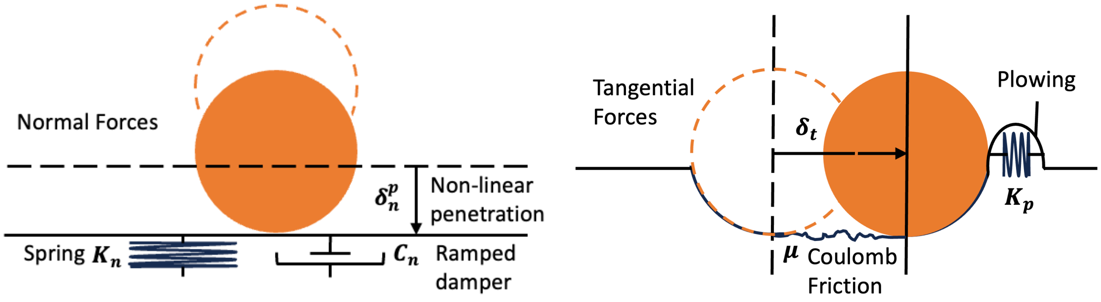

Figure 11. Contact model visualization.

The normal component of Zupp's simplified model generalizes to a Hertzian-type penalty law.[17] The general form includes an exponent, p, on the penetration term, δ_n^p, which for this application can be interpreted as a soil compaction parameter. When the compaction exponent is greater than one, the response stiffens with increasing penetration as deeper material is engaged. A damping term, $C_n\dot{\delta}_n$, can be included in the same framework to represent dissipative effects from contact inelasticity. Figure 11 provides a visual depiction of the full generalized model used in the present simulation. The mathematical model is as follows:

$$F_n = \begin{cases} w_b w_r (K_n \delta_n^p + w_d C_n \dot{\delta}_n), & \delta_n > 0 \\ 0, & \delta_n \leq 0 \end{cases} \tag{6}$$

$$F_t = \mu F_n + K_p \delta_t$$

where setting the compaction exponent to 1 and the damping coefficient to 0 recovers the Zupp implementation. This model only generates forces if the footpad point is beneath the surface. Forces are always in directions away from the surface. The additional weighting terms w_d, w_b, and w_r, are explained below.

The Hertzian damping term in the above equation is heavily inspired by the MSC Adams IMPACT contact model.[18] The IMPACT model introduces a penetration-weighted damping activation ramp which suppresses excessive forces and improves numerical stability at contact onset. The same ramp can also be interpreted as a compaction effect. The Adams activation shape is not available, so a cosine is selected to represent w_d, which ramps from 0 to 1 along the damping activation depth, δ_d.

$$w_d = \begin{cases} \frac{1}{2}\left[1 - \cos\left(\pi \frac{\delta_n}{\delta_d}\right)\right], & 0 \leq \delta_n \leq \delta_d \\ 1, & \delta_n > \delta_d \end{cases} \tag{7}$$

The penalty formulation predicts forces that are a good match during loading but a poor match during unloading. The spring term is energy conserving: if penetration overshoots gravitational equilibrium, stored energy is returned, rebounding the vehicle and driving oscillations. This is guaranteed to occur in the limit of zero-damping, such as in the Zupp implementation. For lunar regolith however, compaction is assumed irreversible: once crushed, the soil should carry the static load without re-accelerating the vehicle away from the surface.

One approach to suppress spring-back is by collapsing the elastic region of the surface to a narrow band above the maximum penetration level. This is achieved by scaling the normal force with a feedback weight, w_b, that depends on the footpad's position within this band. The maximum penetration is latched once a point on the footpad reaches a near-rest condition, defining a new datum, δ_{MAX}. The weight is near 1 at the datum and transitions to near 0 over the prescribed band thickness, b.

$$w_b = \frac{1}{2}\left[1 - \tanh\left(\frac{6}{\mathrm{b}}\left([\delta_n - \delta_{MAX}] - \frac{b}{2}\right)\right)\right] \tag{8}$$

During subsequent unloading, the normal force scales down to the new elastic equilibrium inside the band. The parameter b limits the allowed spring-back distance and unloading impulse for a trade-off in numerical stability. Values for the transition band between 0.1 and 1 mm provide a suitable balance between rebound and robustness.

In practice, a small limit cycle can persist inside the transition band because the damping term acts over an insufficient distance to suppress chatter. A second feedback weight, w_r, further tapers the normal reaction based on a desired residual sink rate, $\dot{\delta}_r$. The weight transitions from near 1 to near 0 as the sink rate decreases from the desired residual to 0.

$$w_r = \frac{1}{2}\left[1 - \tanh\left(\frac{6}{\dot{\delta}_r}\left(\dot{\delta}_n + \frac{\dot{\delta}_r}{2}\right)\right)\right] \tag{9}$$

As with the band thickness, this parameter can stiffen the problem if it is too small. A value of $\dot{\delta}_r = 0.1$ mm/s is small enough that residual footpad rates are negligible over simulation timescales, yet large enough to suppress chatter.

Table 4. Hertzian contact mechanical properties for lunar regolith.

Parameter	Description	Zupp-like	Adams-like	Unit
K_n	Bearing strength coefficient	350,254	150,000	N/m^p
p	Compaction exponent	1.0	1.5	
b	Soil rebound band thickness	0.1	0.1	mm
$\dot{\delta}_r$	Sink rate residual	0.1	0.1	mm/s
C_n	Damping coefficient	0.0	150,000	N·s/m
δ_d	Damping activation depth	0.0	0.1	m
μ	Footpad/surface coefficient of friction	0.33	0.36	
K_p	Plowing force coefficient	1,454	1,454	N/m

The Hertzian contact parameters used in this study are summarized in Table 4. These values were iteratively tuned in MSC Adams using the IMPACT contact model, with the Apollo 11 measurements as the correlation target. Nominal parameters were seeded from internal LM landing-gear LS-DYNA[*] footpad-to-surface impact tests using regolith models with lunar properties. Only minor adjustments to the LS-DYNA values were required to match the expected penetration response under Apollo 11 conditions.

---

[*] LS-DYNA is a commercial, general-purpose finite-element analysis code widely used for high-speed, nonlinear transient dynamics, including contact problems.

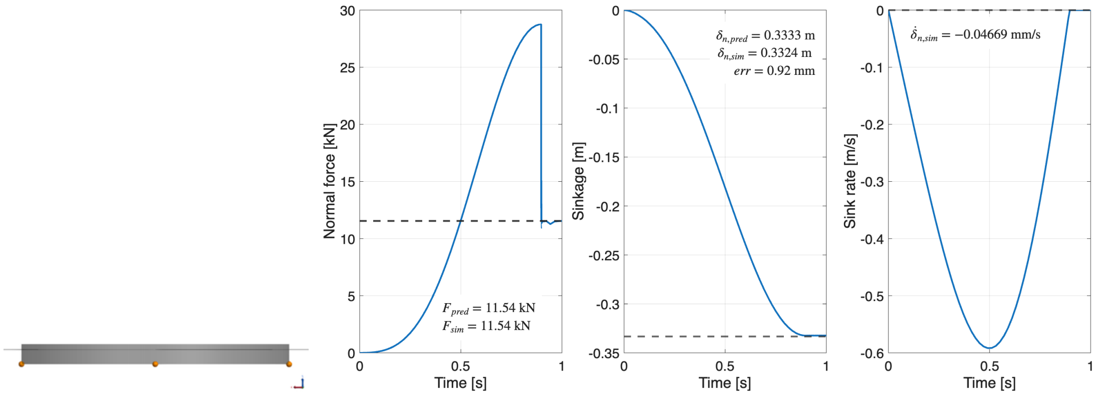

Figure 12. Contact model verification exercise.

Figure 12 verifies the point cloud architecture and the undamped normal contact law with a single footpad drop test under lunar gravity of 1.63 m/s^2. The footpad's mass is that of the total vehicle, 7,063.5 kg, and the soil parameters are tuned to the Adams-like values from Table 4, with the exception that damping is set to 0. The ground normal force at rest is expected to satisfy $F_n = mg$, and conservation of energy can be used to predict the depth of the footpad by relating work done by soil to gravitational potential.

$$\delta_{n,pred} = \sqrt[p]{(p+1)mg/K_n} \tag{10}$$

The simulated response matches with the predicted values of normal force and penetration at rest. The residual sink rate is under the desired value of 0.1 mm/s and the depth at rest is near machine precision to the maximum penetration, both of which are expected from the weighting formulation.

BOUNDING PERFORMANCE

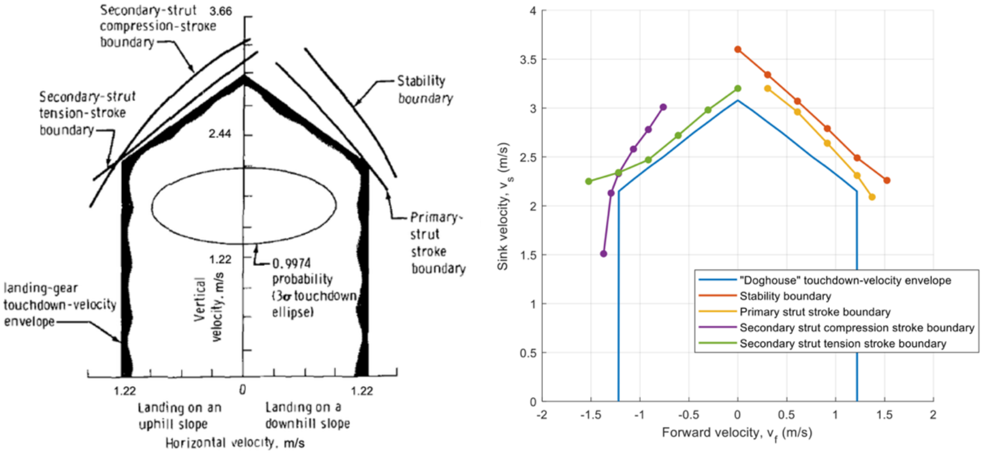

Figure 13. Apollo 11 LM Doghouse, legacy vs. Adams reconstruction.

Part of verifying the landing gear model is establishing consistency with the Apollo "Doghouse." The Doghouse represents the design envelope used to certify allowable combinations of horizontal and vertical impact velocity. The LM Doghouse assumes a relatively steep 12° slope to stress toppling stability and landing gear energy absorption performance. The idea is that when the boundaries that define the invalid scenarios exist outside the Doghouse, scenarios inside the Doghouse represent valid landings with stable attitudes and positive energy absorption margins. These boundaries are generated from engineered cases that are designed to indicate the line at which failures begin to occur. The limiting input scenarios depend upon the subsystem under stress. The following curves are required to be outside the doghouse for design certification: (1) the stability boundary associated with toppling potential, (2) the primary strut stroke boundary, (3) the secondary strut compression stroke boundary, and (4) the secondary strut tension stroke boundary.

A Doghouse reconstruction is not performed in GLASS because the present implementation does not include the terrain complexity required for these exercises. However, the Doghouse is recreated using the high-fidelity MSC Adams model and is included in Figure 13 as an additional verification comparison. Agreement with the heritage Doghouse provides a check that the integrated model reproduces the expected landing stability and stroke limits across the expected impact conditions. The resulting Adams boundary curves compare very well to the Apollo heritage curves, supporting the use of the Adams model as a verification reference for landing stability and energy absorption limits.

APOLLO 11 RECONSTRUCTION

V&V of the fully integrated model consists of comparison to historical flight measurements and modern reconstructions of the Apollo 11 touchdown event. The two reconstructions, Zupp and Adams, have differing assumptions regarding terrain mechanical properties and vehicle-to-ground relative initial attitudes. Initial conditions that can be gleaned from the Apollo Experience Report are shared, while other parameters are the result of iterative tuning by either simulation. Time history comparisons will be made to each independently to prevent clutter in the charts. The flight data time histories are digitized from the Landing Gear Subsystem section of the Apollo Experience Report.

Table 5. Apollo 11 LM reconstruction initial conditions at touchdown.

Parameter	Description	Zupp-like	Adams-like	Unit
V_x	Axial velocity (body frame)	0.5730	0.5740	m/s
V_y	Lateral velocity (body frame)	-0.6147	-0.6481	m/s
V_z	Forward velocity (body frame)	-0.2130	-0.0447	m/s
θ_y	Pitch Euler angle (321 rotation)	0.9430	1.4827	°
θ_z	Roll Euler angle (321 rotation)	2.5450	2.2937	°
θ_x	Yaw Euler angle (321 rotation)	15.09	0.0	°
ω_y	Pitch rate (body frame)	0.0	0.0	°/s
ω_z	Roll rate (body frame)	-2.8648	-2.8648	°/s
ω_x	Yaw rate (body frame)	-0.6188	-0.6188	°/s
θ_{gs}	Ground slope	4.5	4.2	°
θ_{gy}	Ground yaw (slope approach azimuth)	0.0	-12.0	°

Table 5 lists the GLASS initial conditions at touchdown for the two comparison cases. These parameters are taken directly from the respective sources with minor edits for brevity. The shared parameters include the vehicle rotation rates and translational velocities. While the velocities appear different, the kinetic energies are the same; Zupp defines the velocities in a local-vertical/local-horizontal frame attached to the body, so the components are rotated by the vehicle attitude to be expressed in body coordinates for GLASS. Zupp's vehicle attitude is a straightforward reading of the flight reported values at touchdown, while the Adams values are an equivalent form that relies on a value for the ground slope approach azimuth rather than the vehicle yaw angle. For both simulations, the ground slope was determined using a trial-and-error approach by propagating the initial conditions forward and selecting for the slope input that best matches attitude time histories to the historical data. Other differing inputs, such as mass properties and terrain mechanics, are in Table 1 and Table 4, respectively. The Zupp comparison uses the nominal mass properties while the Adams comparison uses the Apollo 11 properties.

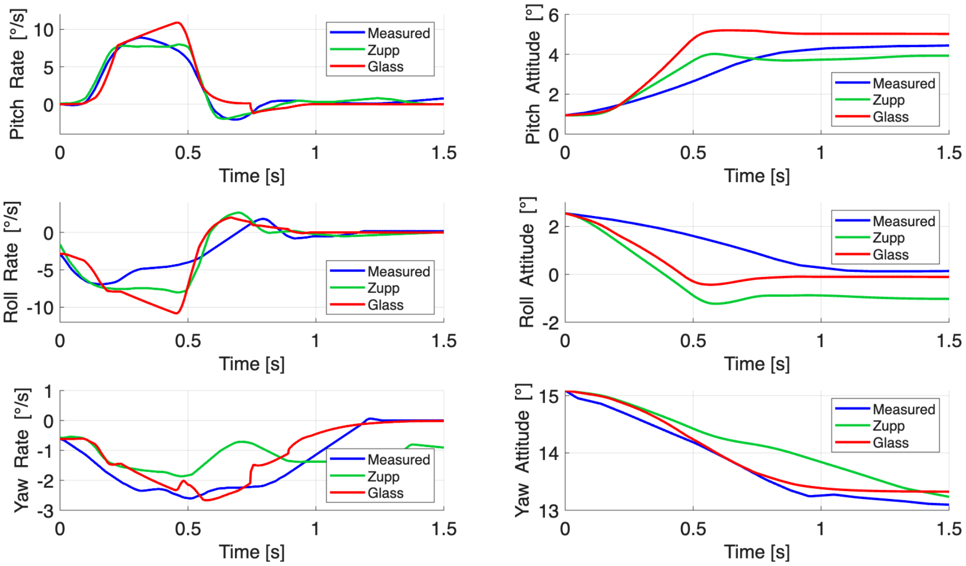

Figure 14. Zupp-like GLASS reconstruction against Zupp and measured.

The Zupp-like GLASS Apollo 11 touchdown results are coplotted with the measured data and Zupp reconstruction in Figure 14. As described in Reference 3, the +Y and +Z footpads contact the surface nearly simultaneously, which initiates a roll-left and pitch-up response. Overall, GLASS agrees well with the comparison data. The angular rate histories evolve in family and settle to similar final attitudes, with the closest agreement occurring in the pitch and roll channels where the motion is largest. The best match to Apollo measured data is in yaw, where GLASS matches the measured peak rate and the time-to-rest more closely than Zupp. The Zupp rate histories lack the transient peaks seen in GLASS, which could suggest more nuance in the contact model or reduced sensitivity to higher-frequency dynamics. These discrepancies are unsurprising, given that the Zupp contact rebound treatment and details of the simulation integrator are unavailable.

Mission photographs suggest that soil penetration was shallow at all four footpads, on the order of 2.0 to 7.62 cm. GLASS is consistent with this observation, predicting a penetration range of 1.93

to 6.68 cm. Mission data also indicate skid distances of up to 7.62 cm, which GLASS reproduces closely with a maximum skid of 7.01 cm.

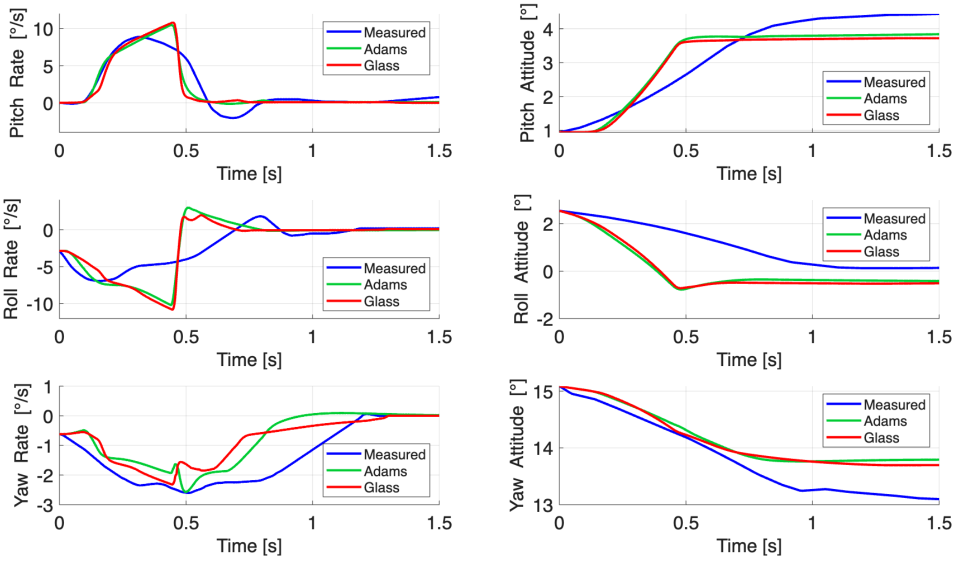

Figure 15. Adams-like GLASS reconstruction against Adams and measured.

Figure 15 coplots the Adams-like attitude response from the GLASS simulation with the Apollo 11 measured data and Adams reconstruction. The sequence of footpad contacts and ensuing vehicle motion are in agreement with the measured data. The GLASS and Adams attitude response are in excellent agreement, most notably in the pitch and roll channels. The linear ramp in the pitch rate response leading up to the steep drop occurs as the vehicle pivots about two planted footpads under constant acceleration motion. The abrupt arrest indicates the moment that the opposite footpads make contact with the surface. The measured rates exhibit softer inflections and appear to be lagging in time, which is consistent with smoothing from a low-pass telemetry filter. GLASS soil penetration levels remain consistent with flight observations, ranging from 4.14 cm to 6.32 cm. The maximum skid distance is slighter lower, reaching up to 4.17 cm, which is to be expected with a higher assumed footpad-to-surface friction.

Table 6. Apollo 11 landing gear strut crush level simulation comparison.

Landing Gear Strut	Photo average	Rogers sim	Zupp sim	GLASS sim (Zupp-like)	Adams sim	GLASS sim (Adams-like)
+Z, primary	0.00	0.00	0.00	0.00	0.00	0.00
+Z, right	--	0.51	0.00	0.00	0.00	0.00
+Z, left	10.16	9.14	4.57	7.01	6.10	4.20
–Z, primary	0.00	0.00	0.00	1.52	0.00	0.00
–Z, right	6.35	8.13	3.81	10.15	9.40	6.00
–Z, left	11.43	0.51	0.00	0.57	0.00	0.00
+Y, primary	0.00	0.00	0.00	0.00	0.00	0.00

+Y, right	7.11	8.64	4.57	10.15	9.14	5.84
+Y, left	1.27	2.54	1.78	1.66	2.29	1.40
–Y, primary	0.00	0.00	0.00	1.52	0.00	0.16
–Y, right	8.13	3.56	2.54	5.89	2.29	1.43
–Y, left	0.00	3.56	3.05	2.55	0.25	0.59
Cumulative Difference	--	25.16	31.25	29.07	27.68	26.59

The final V&V effort is summarized in Table 6, which compares honeycomb crush levels measured from Apollo 11 photography with the various simulation predictions. The photographic measurements have a stated uncertainty of approximately 0.635 cm per measurement. Any values reported under left/right are for secondary struts and should be interpreted as stroke in the tensile direction. The color coding indicates agreement level (blue-high, yellow-medium, red-low) with the photo estimates. The cumulative difference is the sum of the absolute difference of each row with respect to the measured data.

In terms of consistency with the observations, the post-flight Rogers simulation shows the closest overall agreement across the struts, followed by the MSFC GLASS with Adams-like initial conditions, then by the LaRC Adams simulation, then again by the MSFC GLASS but with Zupp-like initial conditions, and finally the Zupp. Most simulations indicate that the secondary struts provide essentially all the energy attenuation. In contrast, the Zupp-like GLASS is the only model that predicts nonzero stroke in the primary struts. Qualitatively, the simulations mostly capture the same relative trends within each leg, where one secondary strut strokes more while the other strokes less. The models agree on which strut is the high or low contributor except for the -Y struts.

The most conflicting measured value is the -Z left secondary strut, which shows significant stroking in the photographic estimate while all simulations predict a near 0 value. This discrepancy underscores that the reconstruction assumptions are limited in certainty and suggests that mismatches elsewhere should be interpreted with such context in mind.

CONCLUSIONS

NASA MSFC has matured a high-fidelity touchdown dynamics capability within the MATLAB® Simulink®/Simscape™ Multibody™-based GLASS framework, using the Apollo Lunar Module as a development test article. The implementation emphasizes lunar regolith-to-footpad interactions, honeycomb shock absorption, and multibody landing-gear linkages. Separate attention is given to solver considerations needed to efficiently and robustly simulate intermittently stiff constrained dynamics using variable-timestep integration in Simulink®/Simscape™. Substantial prior work by the LaRC team using an MSC Adams-based touchdown dynamics tool provided valuable reference cases and lessons learned that informed this effort. Verification and validation include comparison to Apollo 11 flight observations and to modern NASA reconstructions from JSC and LaRC. GLASS compares well to these references, establishing confidence for touchdown risk assessments of commercial architectures in support of NASA's HLS insight program.

REFERENCES

[1] National Aeronautics and Space Administration (NASA), Exploration Systems Development Mission Directorate, *Moon-to-Mars Architecture Definition Document (ESDMD-001)*, NASA Technical Publication NASA/TP-20230002706, April 2023.

[2] M. K. Barker, E. Mazarico, G. A. Neumann, D. E. Smith, M. T. Zuber, and J. W. Head, "Improved LOLA Elevation Maps for South Pole Landing Sites: Error Estimates and Their Impact on Illumination Conditions," *Planetary and Space Science*, Vol. 203, Sept. 2021, Art. 105119. doi:10.1016/j.pss.2020.105119.

[3] National Aeronautics and Space Administration, *NASA Space Flight Program and Project Management Requirements*, NASA Procedural Requirements (NPR) 7120.5F (w/Change 4), Effective Date: Aug. 3, 2021. (NASA Online Directives Information System (NODIS) Library).

[4] T. VanZwieten, M. D. Johnson, J. P. McCullough, and E. T. Gilligan, "Time and Frequency-Domain Cross-Verification of SLS 6DOF Trajectory Simulations," paper presented at the AAS Guidance, Navigation, and Control Conference, Breckenridge, CO, 2014, Rept. M13-2970, Marshall Space Flight Center, Huntsville, AL.

[5] J. Orphee, N. Olson, K. Clements, M. Hawkins, A. Summers, W. Wu, M. Fritzinger, and K. Miller, "Evaluation of Precision Landing Performance Using a Generalized Aerospace Simulation in Simulink Framework." 45th Annual AAS Guidance, Navigation and Control (GN&C) Conference, Breckenridge, CO, 2023. NASA Technical Reports Server, Doc. ID 20230000011

[6] National Aeronautics and Space Administration, *Apollo 11 Mission Report: Preflight, Flight, and Postflight of Apollo 11*, Technical Memorandum (TM), Rept. NASA-TM-X-62633 (also MSC-00171), Manned Spacecraft Center, Houston, TX, Nov. 1969.

[7] Walton Jr., W.C., Herr R.W., and Leonard, H.W., “Studies of Touchdown Stability for Lunar Landing Vehicles,” J. Spacecraft, Vol. 1, 1964.

[8] W. F. Rogers, *Apollo Experience Report – Lunar Module Landing Gear Subsystem*, NASA Technical Note, Rept. NASA TN D-6850 (also MSC S-316), Manned Spacecraft Center, Houston, TX, June 1972.

[9] G. A. Zupp, *An Analysis and a Historical Review of the Apollo Program Lunar Module Touchdown Dynamics*, NASA Johnson Space Center (ret.), unpublished.

[10] R. F. Stengel, "Manual Attitude Control of the Lunar Module," AIAA Guidance, Control, and Flight Mechanics Conference, Princeton, NJ, Aug. 18–20, 1969, AIAA Paper 69-892.

[11] L. Noels, L. Stainier, J.-P. Ponthot, and J. Bonini, "Automatic time stepping algorithms for implicit numerical simulations of non-linear dynamics," *Advances in Engineering Software*, Vol. 33, Nos. 7–10, 2002, pp. 589–603. doi:10.1016/S0965-9978(02)00073-X.

[12] MathWorks, *Simscape Documentation*, Release R2024b, The MathWorks, Inc., Natick, MA, 2024, “Best Practices for Simulating with the daessc Solver.”

[13] MathWorks, *Simulink Documentation*, Release R2024b, The MathWorks, Inc., Natick, MA, 2024, “Choose a Jacobian Method for an Implicit Solver.”

[14] MathWorks, *Simulink Documentation*, Release R2024b, The MathWorks, Inc., Natick, MA, 2024, “Variable-Step Solvers in Simulink — Error Tolerances for Variable-Step Solvers.”

[15] Zupp, Jr., G.A. and Doiron, H.H., “A Mathematical Procedure for Predicting the Touchdown Dynamics of a Soft-Landing Vehicle,” NASA TN D-7045, 1971.

[16] Bendix Corporation, *Lunar Module (LM) Soil Mechanics Study. Final Report.*, Rept. AM-68-1, Energy Controls Division, May 1, 1968.

[17] M. Machado, P. Moreira, P. Flores, and H. M. Lankarani, "Compliant Contact Force Models in Multibody Dynamics: Evolution of the Hertz Contact Theory," *Mechanism and Machine Theory*, Vol. 53, 2012, pp. 99–121.

[18] M. Rostamian, "Contact Modeling in Adams: Detailed Analysis of Contact Parameters and Integrator Settings," *SimAcademy Series* Webinar WM412 (webinar handout PDF), MSC Software, Dec. 19, 2019.